

Efficient heat spreader using supersonically sprayed graphene and silver nanowire

Tae-Gun Kim^{a,1}, Chan-Woo Park^{a,1}, Deok-Yoon Woo^a, Jeehoon Choi^{b,*}, Sam S. Yoon^{a,*}

^a School of Mechanical Engineering, Korea University, Seoul 02841, Republic of Korea

^b LG Electronics Inc., Seoul, Republic of Korea

HIGHLIGHTS

- Supersonically sprayed rGO-AgNW dissipates heat to remediate a line hotspot.
- The effect of film thickness is investigated to identify the optimal thickness of the film.
- The addition of AgNW reduce the overall film thermal resistance.

ARTICLE INFO

Keywords:

Heat dissipation
Graphene oxide
Silver nanowire
Heat spreader
Cooling film
Joule heating

ABSTRACT

Hotspots in high-power and high-density microelectronic devices are a major problem because insufficient thermal dissipation can cause device malfunction. We introduce supersonically sprayed thin films made of reduced graphene oxide (rGO) and silver nanowires (AgNW) that can efficiently dissipate heat to remediate hotspots. Film deposition by cold supersonic spraying provides superior adhesion and requires no post-deposition treatment, making it compatible with a wide range of surface materials. A rGO film heat spreader is deposited on an Al₂O₃ substrate (10 × 10 cm²), which is Joule-heated using a nickel–chrome wire. Heat quickly dissipates over the entire surface due to the rGO film, eliminating the localized hotspot. The effect of film thickness is investigated to identify the optimal thickness of the deposited rGO film heat spreader. The cooling capability of pure graphene oxide films is characterized and compared to the heat dissipation performance of a hybrid rGO–AgNW film and an uncoated substrate. The morphology and surface properties of the films are characterized using scanning electron microscopy, Raman spectroscopy, optical profilometry, and thermal infrared imaging. An rGO film thickness of 10 μm produced the lowest thermal resistance and the addition of AgNW enhanced film thermal performance by reducing the thermal resistance.

1. Introduction

Power electronics devices and systems associated with the efficient generation, transmission, and conversion of electrical energy are widely used in public transportation, hybrid and electric vehicles, home appliances, industrial energy storage, telecommunications, and the photovoltaic industry. These power systems use semiconductor devices which are vulnerable to heat. These systems are generally composed of silicon substrates, silicon carbide, gallium nitride, printed circuit boards, lead frames, and electrically insulating ceramic substrates [1–12]. The amount of heat generated by power electronics has been steadily rising because of increasing device miniaturization. Miniaturization has increased continuously to facilitate device portability while

device functionality has multiplied, in turn requiring greater power inputs. Heat flux across these miniaturized devices has increased dramatically, thus increasing the probability of heat-induced malfunctions [13].

Typically, miniaturized heat sinks are attached to power electronics with a thermal interface material (TIM) layer in between. The TIM layer fills irregular air gaps between the electronic components and the heat sink for efficient heat transport [3–5,7,8,10]. However, the TIM layer itself can be insulating, preventing efficient heat dissipation [14]. To reduce the thermal resistance of the TIM layer, additives with superior thermal properties such as silver, graphene, carbon nanotubes, polymers, and nanoscale alumina have been utilized [15–21]. However, this strategy has limited applicability because of the complicated chemical

* Corresponding authors.

E-mail addresses: choijeehoon@gmail.com (J. Choi), skyoony@korea.ac.kr (S.S. Yoon).

¹ These authors have contributed equally.

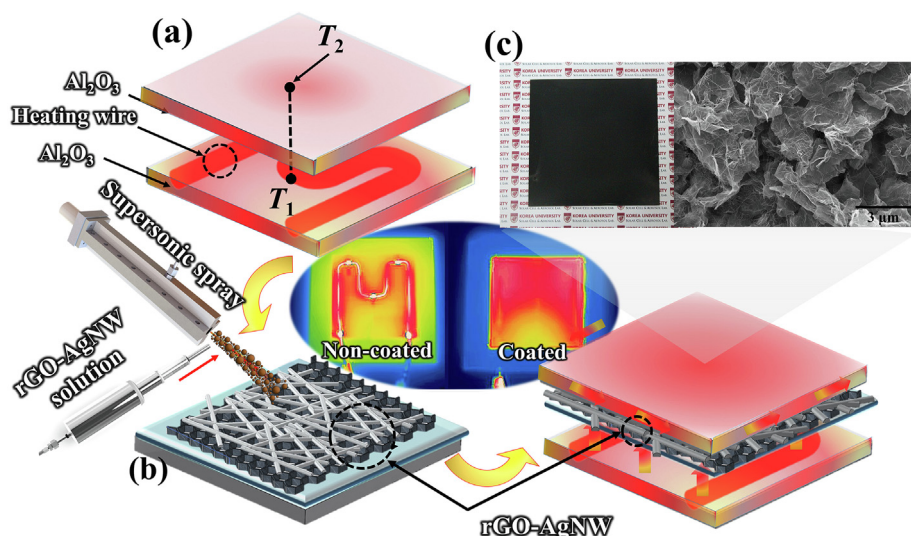


Fig. 1. Detailed schematic of the cooling test module. (a) Heating wire sandwiched between Al₂O₃ substrates. (b) Heat spreader inserted between the substrates. (c) Top view of the fabricated rGO-AgNW heat spreader. Note that the top surface is also coated.

processing and deposition of TIMs, poor compatibility with many surfaces, limited reliability of composites, and high cost of additives.

System integration design, miniaturization, and the installation of heat sinks for power electronics are costly processes that ultimately hinder the commercialization of these conventional technologies. Therefore, an alternative cooling method must be developed. The fabrication of cooling mats or films that can be directly mounted on an electronic device provides a commercially viable solution. This strategy only requires materials with good thermal properties and a scalable coating method for the quick deposition of heat-spreading materials onto device surfaces.

Graphene is known as an efficient hotspot-removing material and heat spreader [22–26]. Baladin et al. [27] showed that the thermal conductivity of a suspended single-layer graphene sheet can approach ~5300 W/m-K, while Seol et al. [28] demonstrated that the thermal conductivity of single-layer graphene mounted on a SiO₂ surface is ~600 W/m-K, which is higher than that of copper thin films (~250 W/m-K). These studies revealed that graphene is a good candidate material for transporting and dissipating heat. On the other hand, the thermal conductivity of silver nanowires (AgNWs) is ~380 W/m-K at room temperature, indicating their utility as a heat spreader [29].

Herein, we fabricate heat-spreading films by spray-coating a mixture of reduced graphene oxide (rGO) and AgNWs. This rGO-AgNW hybrid film can enhance heat transport while forming various textured surfaces which can act as heat sinks by increasing the total surface area. In limited spaces such as those in miniaturized devices, nanotexturing offers a viable solution for increasing surface area to enhance the overall cooling performance [13]. To the best of our knowledge, graphene-AgNW hybrid films have been used as Joule heating materials, but not as heat spreaders [30–32].

Furthermore, we demonstrate the deposition of rGO-AgNW hybrid films via supersonic cold spraying, which has never been done. Using this method, the materials are compactly deposited to minimize the presence of highly thermally resistive air pockets between deposited layers. Supersonic spraying is performed in open-air conditions, avoiding the need for vacuum chambers, thus beneficially reducing manufacturing costs. Film densification is achieved simply by supersonic impact. Moreover, post-treatment for film densification is not necessary. This permits the use of flexible substrates which would otherwise be impossible because of the vulnerability of flexible substrates to high temperature processes. Overall, the deposition method we introduced herein is unique and provides many manufacturing and thermal performance advantages [33–38].

2. Experimental methods

2.1. Supersonic spraying

The supersonic cold-spraying system comprises a gas compressor, converging-diverging nozzle (De Laval nozzle), gas heater, atomizer, and syringe pump [33–37]. Air is compressed up to 0.4 MPa by the gas compressor, heated at 250 °C by passing through the gas heater, and then supplied to the nozzle to develop a supersonic flow. The supersonic flow is deposited on the ceramic substrate simultaneously with the rGO (and AgNW) dispersion which is supplied by the atomizer.

The rGO dispersion is prepared by adding 0.25 g of rGO (Average length is approximately < 10 μm and thickness of < 1 nm, N002-PDR, Angstrom Materials) to a precursor solution comprising 40 mL of *N,N*-dimethylformamide (DMF, Sigma-Aldrich) and 0.3 mL of 8 wt% polyacrylonitrile (PAN; Sigma-Aldrich, average *M_w* of 150,000). The resulting dispersion is injected by a syringe pump (Legato 210, KDS) at a flow rate of 1.5 mL/min to an atomizer (VCS 40 kHz, Sonics & Materials). The AgNWs (Average diameter is 20 nm and length is 15 μm) are dispersed in 40 mL of isopropyl alcohol (IPA, Duksan, Korea) at a concentration of 0.15 wt%. This rGO/AgNW mixture ratio was selected to sufficiently cover rGO flakes with AgNWs, which was visually confirmed by SEM images; this optimal mixture ratio was found by trial-and-error. Supersonically sprayed rGO/AgNWs provide superior adhesion on various types of substrates. As an example, AgNWs were supersonically sprayed on a flexible PET substrate. In a peeling test, 3 M scotch tape was repeatedly attached to and detached from the supersonically-sprayed AgNWs film up to 30 times, with no significant variation in sheet resistance after the first cycle of detachment, according to our previous studies [36].

2.2. Heat spreader fabrication

Fig. 1 shows a schematic of the fabrication procedure for the heat spreader. The antenna-shaped nickel-chrome heating wire is sandwiched between two Al₂O₃ substrates. The heating wire is supplied with 10–30 W power from a direct current (DC) supply. A thermocouple is attached directly on the heating wire at T₁ as indicated in Fig. 1(a), and another is attached right above T₁ on the top surface (T₂) of the top substrate. Fig. 1(b) depicts the deposition of rGO-AgNW dispersion onto the substrate by supersonic spraying. Fig. 1(c) shows the heat spreader coated with rGO-AgNW and a scanning electron microscopy (SEM) image of the top view of the coated surface. The rGO flakes are

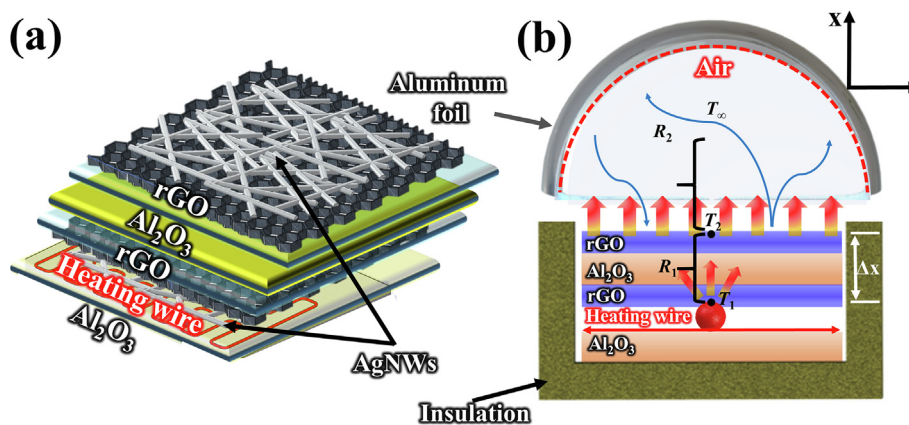


Fig. 2. Detailed schematics of (a) the heat spreader comprising multiple layers of rGO and AgNW films. (b) The insulated heat spreader used in the heat transfer experiment.

covered uniformly with AgNWs. Both the top and bottom sides of the upper Al_2O_3 substrate are coated with rGO–AgNW layers, as described in Fig. 2(a). This coating on both sides is purposely designed to facilitate the removal of hotspots by spreading heat throughout the substrate.

2.3. Heat transfer experiment

A DC power supply with a maximum output of 60 W (E3644A, Agilent Tech, US) was used to supply 10–30 W heating power. The measured accuracies of the supplied voltages and currents are $0.1\% \pm 150 \text{ mV}$ and $0.1\% \pm 15 \text{ mA}$ respectively. The nickel-chrome heating wire has a resistance of $5.73 \Omega/\text{m}$ and a diameter of 0.5 mm. The DC voltage was applied to the nickel-chrome wire sandwiched between the Al_2O_3 substrates. All temperatures (T_1 and T_2) were recorded using a temperature data logger (GL-240, Graphtec, US). The overall uncertainty of temperature measurements using K-type thermocouples (probe size of $1 \times 150 \text{ mm}$) was estimated to be $\pm 0.5^\circ\text{C}$. Based on the repeatability of the data, the overall uncertainty level of the amount of the heat transferred to the wire was estimated to be 1.6% using an error propagation method [39]. The thickness of the rGO–AgNW layer was $\sim 5\text{--}17 \mu\text{m}$, depending on the number (N) of spraying sweep passes ($5 \leq N \leq 20$). The heat was transferred through the upper layers while the bottom substrate was insulated to minimize the heat loss (see Fig. 2(b)). The conduction heat loss through the bottom substrate, estimated from the temperature difference between the bottom substrate and the insulation was less than 1%. On the top surface of the heat spreader, the surrounding environment stimulated convective cooling. The radiative loss was minimized by covering the heat spreader with an aluminum foil, as depicted in Fig. 2(b).

This study used ASTM E1461 (ASTM international, thru-plane) as a common method for measuring the thermal conductivity of sandwich structure samples along the vertical direction. In this method, the thermal conductivity can be calculated by measuring the thermal diffusivity, which can be estimated using the following equation: $k \sim \lambda \cdot \rho \cdot C_p$, where λ the thermal conductivity, ρ the density, and C_p the specific heat capacity. The measurable range is 0.1–2000 W/m·K.

2.4. Characterization

High-resolution SEM (HR-SEM at 15 kV, XL30 SFEQ, Phillips Co., Netherlands) and a non-contacting 3-D optical profiler (NT, Veeco, USA) were used to measure the morphology and roughness of the surface of the multilayer heat spreader. An infrared (IR) camera (FLIR-E63900, FLIR System, Inc.) was also used to visualize the transfer of heat over time. The IR camera had a thermal sensitivity of 30 mK at room temperature (25°C) with an uncertainty level of about $\pm 1\%$. An

initial calibration of the IR camera was carried out by measuring the temperature of an object at 25°C , whose value was confirmed against the thermocouple measurement. The temperature values from the thermocouple measurement and the IR image were synchronized by adjusting the emissivity value, ϵ . The emissivity of the IR camera was adjusted to $\epsilon = 1$ to avoid heat residues from other surrounding sources.

3. Results and discussion

Fig. 3 compares the heating wire temperatures (T_1) using substrates deposited with pure rGO films of various thicknesses with respect to time. Larger N values correspond to thicker films. $N = 0$ refers to the “bare” non-coated substrate. For $t \geq 600 \text{ s}$, the temperature change is insignificant and T_1 acquired at $t = 2000 \text{ s}$ is in a sufficiently steady state. For all q values, all rGO films cool the heating wire to some degree. For $q = 10 \text{ W}$ in Fig. 3(a), the temperature difference is not significant, although larger N yield lower T_1 by a few degrees Celsius. As the supplied heat is increased to $q = 15 \text{ W}$ in Fig. 3(b), T_1 is the lowest at $N = 10$. The same trend is observed for $q = 20$ and 25 W in Fig. 3(c) and (d) respectively; T_1 is the lowest at $N = 10$. It is interesting to note that T_1 at $N = 20$ is higher than T_1 at $N = 5$ for $q = 15, 20$ and 25 W . This indicates heat insulation because of the excessive thickness of the coating. Except for $N = 20$, all rGO films ($N = 5$ and 10) overall produce lower T_1 . One should keep in mind that there appears to be an optimal coating thickness that renders the most efficient cooling. Measurement uncertainties were explained in detail in Section 2.3.

Fig. 4 compares the IR images of the heated bare ($N = 0$), rGO coated ($N = 10, 20$), and rGO–AgNW hybrid film-coated substrates. The nickel-chrome heating wires follow a curved path and are sandwiched between the Al_2O_3 substrates. The electrical current inlet and outlet are observed at the bottom of the substrates. Once the electrical voltage is supplied through the circuit, Joule heating begins with $q = 20 \text{ W}$.

The temperature gradually rises and the region right above the heating wire heats up first, the evidence of which is clearly visible in the IR images for all cases. Then, the heat spreads over the entire substrate. At $N = 0$ (the bare case) in Fig. 4(a), the heat is highly concentrated above the heating wire and poorly distributed over the surface; the hotspots remain over time and are clearly visible with the highest temperatures localized near the heating wire. At $N = 10$ in Fig. 4(b), the heat is well distributed over the surface, indicating the utility of the rGO layer as an efficient heat spreader. When the rGO layer thickness is further increased to $N = 20$ in Fig. 4(c), heat dispersion is hindered. This is caused by the rGO layer acting as an insulator at an excessive layer thickness. As a result, the substrate temperature above the heating wire in the $N = 20$ case is greater than that acquired with $N = 10$, as previously demonstrated in Fig. 3. For $q = 15, 20$, and 25 W , the

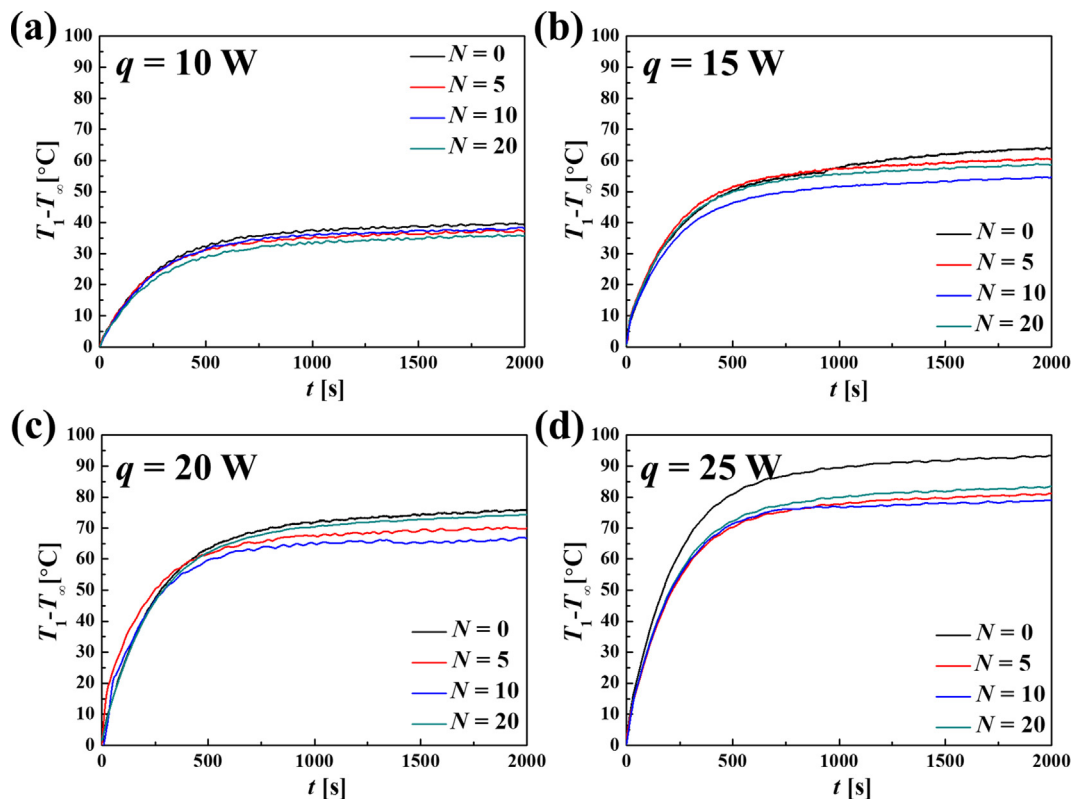


Fig. 3. The heating wire temperature (T_1) vs. time. The effect of the number of spray passes (N) for various heating powers (a) $q = 10$ W, (b) 15 W, (c) 20 W, and (d) 25 W.

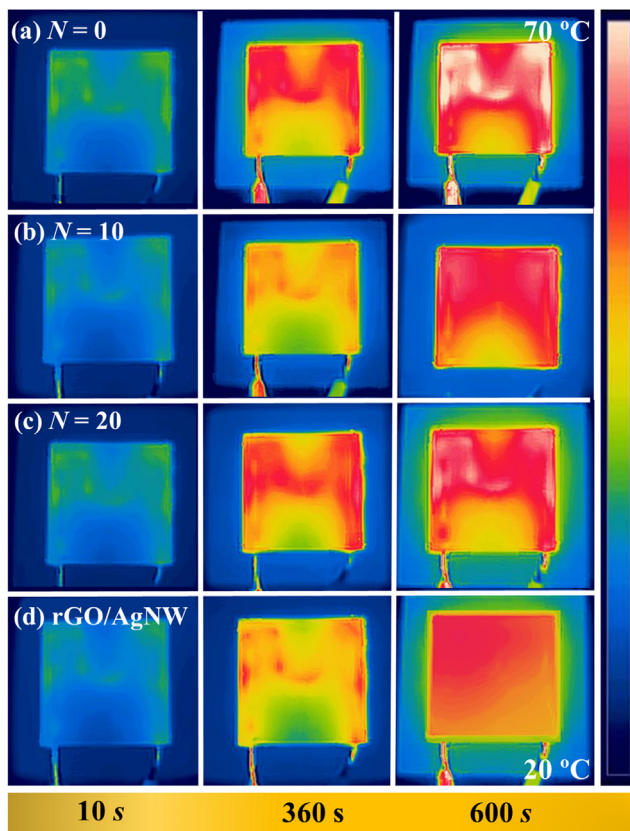


Fig. 4. IR images of heated rGO films for (a) $N = 0$, (b) $N = 10$, (c) $N = 20$, and (d) $N = 10$ with AgNW at $q = 20$ W.

$N = 20$ case yields greater T_1 (lesser cooling) than that from $N = 10$. In addition, Fig. 4(d) shows the heat spreading capability of the hybrid film composed of rGO and AgNWs. It should be noted that this hybrid case has the coating thickness of $N = 10$; thus, it is comparable to the rGO case in Fig. 4(b). Clearly, the heat spreading of these two cases are comparable and superior to the other cases of $N = 0$ or 20. In addition, the heat spreading behavior of the hybrid case appears to be more uniform than the pure rGO case (compare Fig. 4(b) and (c)). This superior heat spreading capability of the hybrid film confirms the thermal enhancement rGO films by AgNWs.

Fig. 5 compares the SEM and OP images acquired from the $N = 0, 5, 10,$ and 20 rGO films. Fig. 5(a) shows images of the bare Al_2O_3 substrate with no rGO deposited. The surface roughness, R_a , of bare Al_2O_3 substrate is $\sim 0.33 \mu\text{m}$. With increasing N , the rGO film thickness increases up to $\sim 16 \mu\text{m}$ for $N = 20$. The OP results also indicate that the surface roughness also increases for increasing N , because the randomly deposited rGO flakes create sharp edges on the film surface. The in-plane thermal conductivity of the rGO film can be enhanced by the increase in the surface roughness. Therefore, the increased roughness can be advantageous in dissipating heat because texturing increases the surface area and thereby promotes efficient convective cooling. However, if the heat transport is hindered by the under-layer thickness, the top surface texturing is useless, which is the case for $N = 20$. A thicker film decreases the influence of the thermal boundary resistance, and the heat transport constriction decreases the through-plane thermal conductivity of the rGO film.

Fig. 6 shows the Raman (532 nm laser excitation) spectra of rGO and rGO/AgNW composite samples. The D band peak (1337 cm^{-1}) is attributed to the inherent defect or disorder in carbon. The D peak shows the breathing mode with a molecular orbital of the A_{1g} symmetry. The G band peak (1580 cm^{-1}) is associated with the phonon vibration of sp^2 -hybridized carbon with E_{2g} symmetry [40]. The narrow D and G bands confirm the existence of graphene sheets in both samples [33]. In Fig. 6(b), the rGO/AgNW Raman spectrum shows redshifted D

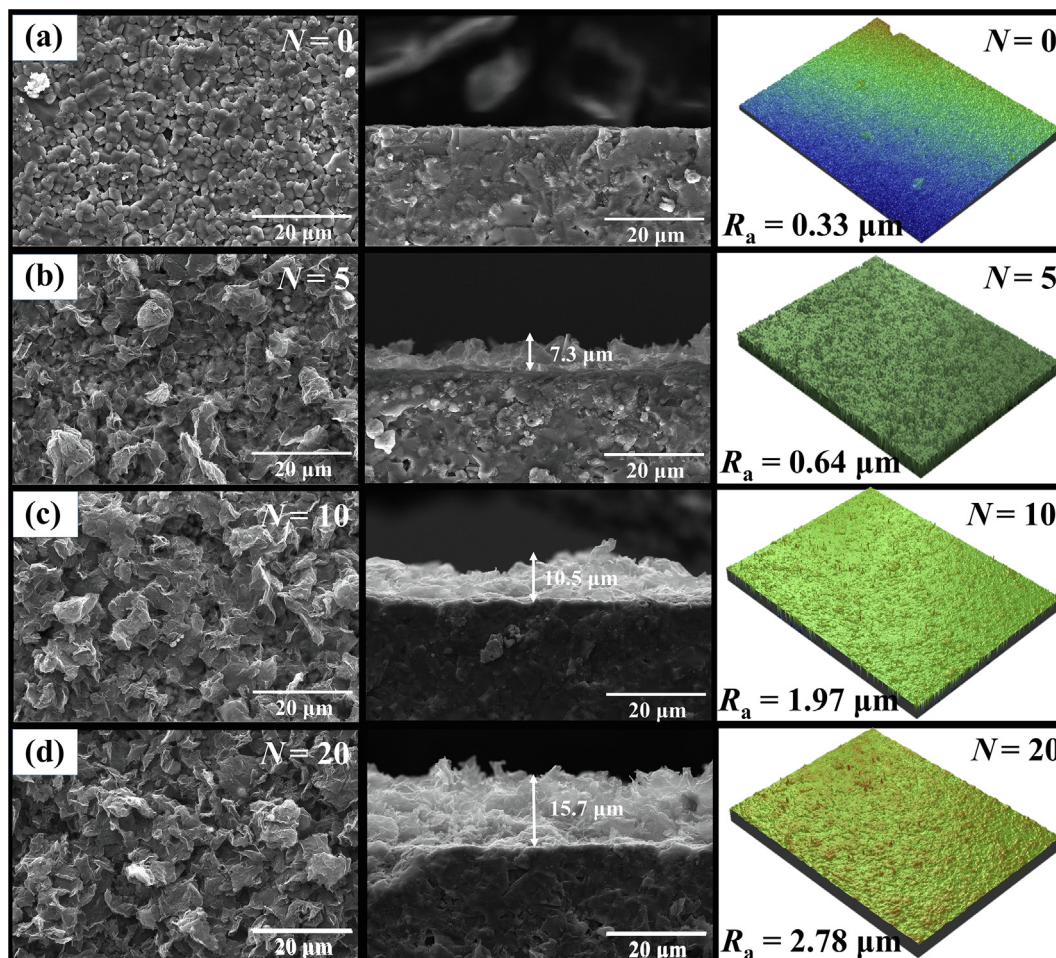


Fig. 5. SEM (left: surface, and middle: cross-section) and optical profiler (OP) images for (a) $N = 0$, (b) 5, (c) 10, and (d) 20.

(1352 cm^{-1}) and G (1587 cm^{-1}) peaks. These redshifts indicate superior adhesion of the AgNWs on rGO flakes (see the inset SEM image in Fig. 6(b)). The I_D/I_G ratio of rGO/AgNW films decreased to 1.28 from the I_D/I_G ratio of 1.38 for pure rGO due to the intermingled AgNWs on rGO flakes. This reduction in I_D/I_G can be regarded as “healing” as the inherent defect of the I_D peak is relatively less intensified. This type of healing occurs due to the metallic support of AgNWs [33]. The surface-enhanced Raman scattering effect of AgNW inclusion [41,42] is visibly confirmed by the doubling in peak intensity compared to the pure rGO sample, as seen in Fig. 6.

Fig. 7(a) shows the electrical circuit model of the thermal resistance

across the rGO- Al_2O_3 -rGO solid layers (from T_1 to T_2) and the convective cooling (from T_2 to T_∞) in the vertical direction. The heating wire is a linear heat source and thus the heat transport phenomenon across the film occurs in all three-dimensional directions in reality. However, to simplify the analysis, a quasi-1D analysis is assumed from T_1 to T_∞ in the vertical direction. As illustrated in Fig. 2(b), the heating system is well insulated; therefore, it is assumed that no heat is lost through the bottom area. Then the total heat supplied, q , is distributed across the axial (x) direction. The heat transported in the axial direction passes through the solid layers and finally open air, for which Fourier’s law and Newton’s cooling law can be used, respectively. The open-air

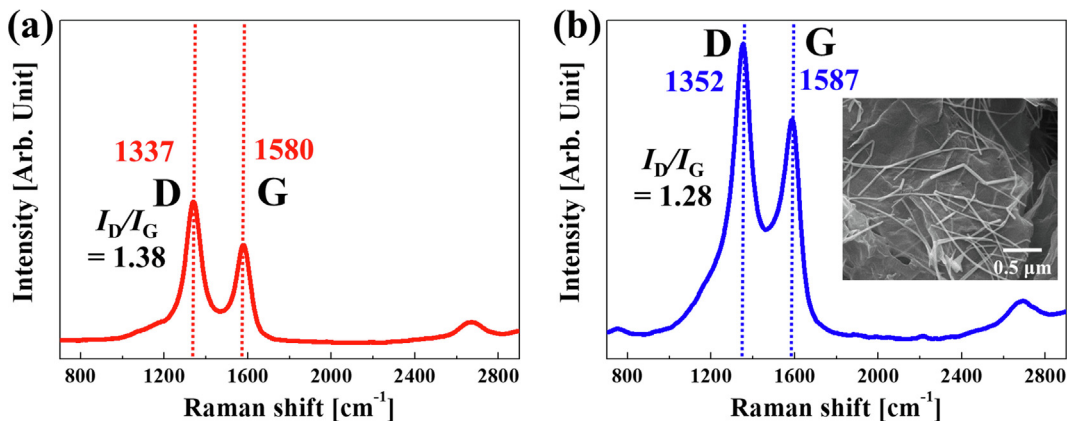


Fig. 6. Raman spectra of (a) rGO and (b) rGO/AgNW films.

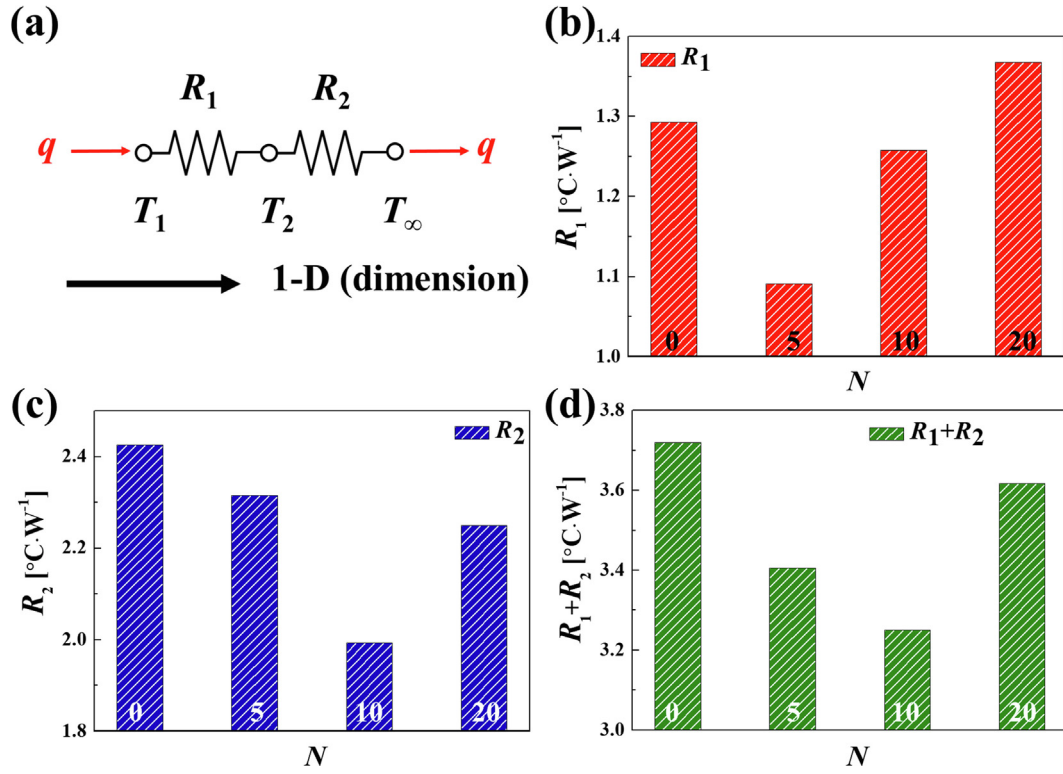


Fig. 7. (a) Electrical circuits depicting the “average” thermal resistance across the solid layers (from T_1 to T_2), and convective cooling (from T_2 to T_∞) in the vertical direction. (b) The relative thermal resistance through the solid layers (alumina and rGO), R_1 . (c) The relative thermal resistance through an open-air medium, R_2 . (d) Sum of R_1 and R_2 . The thermal resistance is averaged over all values of $q = 10, 15, 20$, and 25 W .

space is covered with an aluminum foil to minimize radiative heat loss. Because the film surface temperature remains under 100°C , it is assumed that the radiative loss is insignificant. Therefore, on the film top surface, the heat is lost through convection only; $q \sim h_{\text{eff}} A_p (T_2 - T_\infty)$. Heat transfer through the solid layers is modeled as $q \sim k A_p (T_1 - T_2) / \Delta x$, where h_{eff} (in $\text{W}/\text{m}^2 \cdot \text{K}$) is the effective convective heat transfer coefficient, A_p is the projected surface area (m^2), k is thermal conductivity (in $\text{W}/\text{m}\cdot\text{K}$), and Δx (in m) is the thickness of the solid layers. These can be expressed in terms of the thermal resistance, R , as below:

$$q = \frac{T_1 - T_2}{R_1}, R_1 = \frac{\Delta x}{k A_p} \quad (1)$$

$$q = \frac{T_2 - T_\infty}{R_2}, R_2 = \frac{1}{h_{\text{eff}} A_p} \quad (2)$$

Therefore, the thermal resistance, R_1 and R_2 both have the unit of $^{\circ}\text{C}/\text{W}$ or $[\text{K}/\text{W}]$, introducing the units of thermal conductivity, k , and convective heat transfer coefficient, h_{eff} , are $[\text{W}/\text{m}\cdot\text{K}]$ and $[\text{W}/\text{m}^2\cdot\text{K}]$. By equating Eqs. (1) and (2), the following expression is also obtained:

$$q = \frac{T_1 - T_\infty}{\sum R_i} = \frac{T_1 - T_\infty}{R_1 + R_2} \quad (3)$$

Eqs. (1) and (2) can be estimated below:

$$R_1 = (T_1 - T_2) \times q^{-1} \quad (4)$$

$$R_2 = (T_2 - T_\infty) \times q^{-1} \quad (5)$$

Eqs. (4) and (5) can be estimated because T_1 , T_2 , and q are measured from experiments. These relations are used for the relative comparisons made in Fig. 7. (The temperature is converted from Kelvin to Celsius in the comparative graphs).

Fig. 7 compares the thermal resistances estimated at various thicknesses (N) of the coated rGO layers and the total power input, q . In Fig. 7(b), the thermal resistance through the solid layers is shown (R_1).

The thermal resistance is lowest at $N = 5$. At $N = 20$, the resistance is increased because the coating tends to behave like a thermal insulator when excessively thick. In Fig. 7(c), the cooling of the top surface by convective heat transfer is most efficient at $N = 10$ with the lowest R_2 value. The thermal resistance through air (R_2) decreases with increasing N up to $N = 10$, indicating that the surface area increases by rGO flake texturing indeed promotes convective cooling. However, at $N = 20$, R_2 increases back. In Fig. 7(d), the sum of R_1 and R_2 is plotted, reflecting the total thermal resistance in the axial direction. The total resistance is lowest for $N = 10$. Therefore, the film thickness of $N = 10$ appears to be the most optimal, promoting efficient heat transport for all values of q .

The introduction of AgNWs on rGO flakes was achieved by mixing separate dispersions of rGO and AgNWs; hereafter, the resulting film is called a hybrid film. The hybrid film thickness was set to about $10 \mu\text{m}$ to mimic the benchmark case of $N = 10$, as shown in Fig. 5(c). The purpose of this hybrid design is to increase the thermal conductivity of the coating materials and to determine its effect on the thermal resistances R_1 and R_2 . Fig. 8(a) compares the hybrid film against the benchmark (pure rGO) case of $N = 10$ and the bare case ($N = 0$). It is apparent that the coated films indeed produce lower thermal resistances, as the coating layer promotes both conductive (R_1) and convective (R_2) heat transfer. For conductive heat transfer, the inclusion of AgNWs on the rGO flakes decreases the thermal resistance R_1 , which appears to be reasonable because the thermal conductivity of AgNW is much larger than that of rGO. The morphology of AgNWs on the rGO flakes is shown in Fig. 8(b)–(d). Thus, having AgNWs as thermal conductivity boosters is indeed useful in reducing R_1 . However, the inclusion of AgNW has little effect on R_2 , which is an indicator for the convective cooling process on the top surface exposed to air. Convective cooling is more influenced by the textured surface area (or morphology) than by the material itself. An et al. [13] showed that copper oxide with increased surface area was more efficient in convective cooling than pure copper with a less textured surface. This finding may appear to be counter-intuitive because the thermal conductivity of pure copper is much

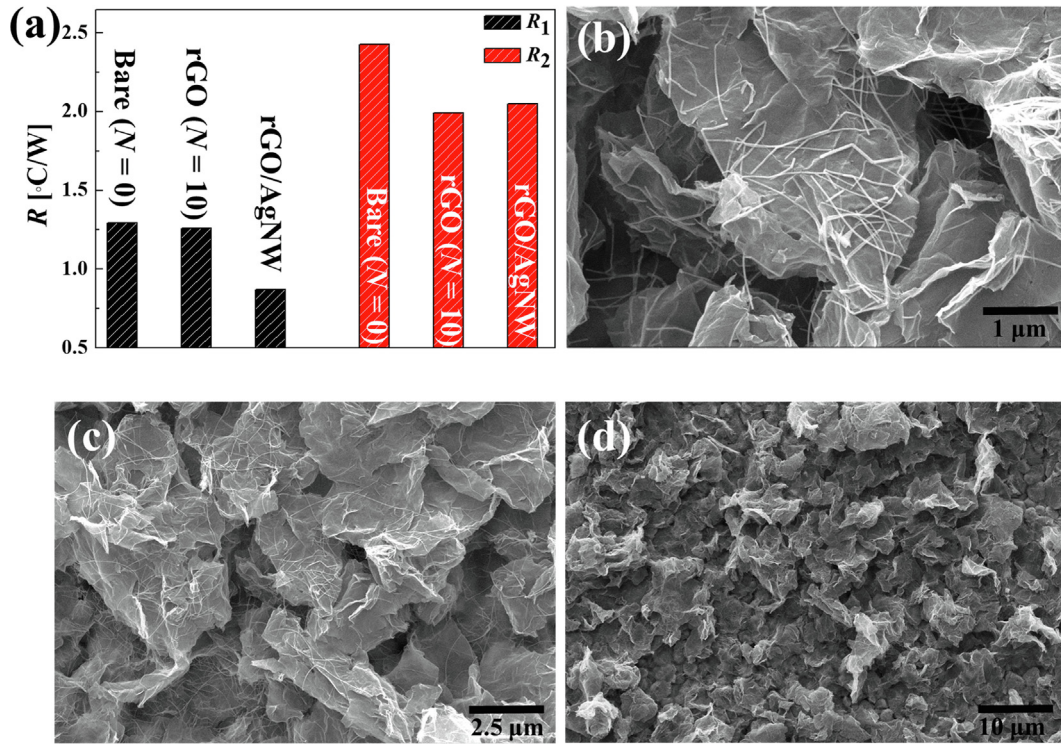


Fig. 8. (a) The thermal resistances (R_1 and R_2) of the hybrid film consisting of rGO and AgNW, shown by SEM images in (b)–(d).

greater than that of copper oxide. However, the surface area (or texturing) dominates the convective cooling process. The length-scale of the AgNWs is much smaller than that of the rGO flakes. The surface area is dominated by rGO flakes while the AgNWs have little influence on the overall surface area. Therefore, the inclusion of AgNWs on the rGO flakes has no influence on convective cooling.

Table 1 compares the effective heat transfer coefficients (h_{eff}) in natural convection (h_{eff}) in the unit of $[\text{W}\cdot\text{m}^{-2}\cdot\text{K}^{-1}]$ and the product of thermal resistance (R_2) and the projected substrate area (A_p), whose unit is $[\text{m}^2\cdot\text{K}\cdot\text{W}^{-1}]$. This effective convective heat transfer coefficient is defined as

$$h_{\text{eff}} = \frac{q_{\text{supp}}}{A_p(T_2 - T_\infty)} \quad (6)$$

The square substrate has 10 cm sides; thus, the projected layer area is $A_p = (0.1 \text{ m})^2$. T_2 is the temperature of the top surface, and T_∞ is the ambient temperature. While considering a heating wire without any substrate on top, the actual supplied heat flux (q_{supp}) to the wire can be estimated as

$$q_{\text{supp}} = h_b A_w (T_1 - T_\infty) \quad (7)$$

Here, h_b is the heat transfer coefficient of the *bare* case (from the heat source), which can be found using the Nusselt number. Temperature T_1

Table 1

Effective convective heat transfer coefficients of rGO films of various thicknesses and rGO/AgNW hybrid films. Note that R_2 herein represent the value estimated using not q of Eq. (5), but q_{supp} of Eq. (6). Thus, R_2 here is different from R_2 of Figs. 7c and 8a.

Material	$h_{\text{eff}} [\text{W}\cdot\text{m}^{-2}\cdot\text{K}^{-1}]$	h_{eff}^{-1} or $R_2 A_p [\text{m}^2\cdot\text{K}\cdot\text{W}^{-1}]$
$N = 0$	7.9	0.13
$N = 5$	8.4	0.12
$N = 10$	10.1	0.10
$N = 20$	8.3	0.12
AgNW/rGO $N = 4$	8.6	0.11
AgNW/rGO $N = 10$	7.7	0.13

is the temperature of the heating wire (99.4 °C). Temperature T_∞ is the ambient temperature (25 °C). A_w is the wire surface area; thus, $A_w = \pi d L$, where d is the wire diameter and L is the wire length, in this case $d = 1 \text{ mm}$ and $L = 0.45 \text{ m}$. The thermal conductivity of air is $k = 0.0289 \text{ W/m}^2\cdot\text{K}$ at the film temperature $T_f = (T_1 + T_\infty)/2 = 62.2 \text{ °C}$. The value of h_b is found using the dimensionless Nusselt number (Nu) as $h_b = Nu k/d$. The Nusselt number in natural (or free) convection from a horizontal cylinder (heating wire) is found from the following expressions involving the Grashof (Gr) and Prandtl (Pr) numbers:

$$Gr Pr = g\beta(T_1 - T_\infty)d^3 Pr/\nu^2 \quad (8)$$

$$Nu = 1.02(Gr Pr)^{0.148} \quad (9)$$

Here, g is the gravitational acceleration (9.81 m/s^2) and β is the thermal expansion coefficient of air defined as $\beta = 1/T_f = 0.003 \text{ K}^{-1}$. The Prandtl number (Pr) and the kinematic viscosity of air (ν) at T_f are 0.7202 and $0.00001896 \text{ m}^2/\text{s}$, respectively. From Eqs. (7)–(9), the heat supply rate of $q_{\text{supp}} = 3.87 \text{ W}$ was obtained. Using this value of q_{supp} in Eq. (6), the values of h_{eff} are obtained as listed in Table 1. The largest h_{eff} (or lowest thermal resistance) corresponds to the optimal rGO case of $N = 10$.

It is noteworthy that according to Eq. (6)

$$T_2 = T_\infty + \frac{q_{\text{supp}}}{h_{\text{eff}} A_p} \quad (10)$$

at a fixed heat supply rate q_{supp} , the surface temperature, T_2 , can be significantly reduced either by a significant increase in the heat transfer coefficient h_{eff} or a significant increase in the surface area A_p . The latter is the case herein, which was achieved by surface texturing via super-sonically sprayed rGO flakes.

The R_1 values compared in Fig. 7(b) are the thermal resistances of the Al_2O_3 substrate covered with an rGO layer. Using the Fourier law, the thermal conductivity of the Al_2O_3 /rGO layers is estimated to be $k \sim (q/A_{\text{wire}})(\Delta x/\Delta T)$, which yields $k \sim 20 \text{ W/m}\cdot\text{K}$ when $q = 10 \text{ W}$, $A_{\text{wire}} = 0.5 \text{ mm} \times 0.1 \text{ m} = 5 \times 10^{-5} \text{ m}^2$, $\Delta x = 1 \text{ mm}$, and $\Delta T = 10 \text{ K}$. This thermal conductivity may vary from standard alumina values in

Table 2
Thermal conductivity (K).

Material	K [W·m ⁻¹ ·K ⁻¹]	Δx [m]	Film thermal resistance [m ² ·K·W ⁻¹]	Testing method	Reference
rGO-AgNW	0.08	1.0×10^{-4}	1.25×10^{-3}	ASTM E1461	Present study (normal)
GnP	0.23	1.0×10^{-3}	4.35×10^{-3}	Hot-wire	[43] (normal)
Carbon nanofiber	1.85	1.0×10^{-2}	5.4×10^{-3}	Hot Disk AB	[44] (normal)
Graphite/Epoxy	6.44	–	1.5×10^{-6}	Fox 50 (LaserComp, Inc)	[20] (in-plane)
2.4 vol% GNP	0.476	–	6.2×10^{-5}		[45] (in-plane)
GnP	1.4	–	$\sim 1.0 \times 10^{-6}$	ASTM C177	[46] (in-plane)
Penetrated flexible graphite	3.8	–	1.3×10^{-6}	ASTM D5470	[47] (in-plane)
Graphene-MLG	14	–	7.1×10^{-5}	Laser flash (NETZSCH)	[19] (in-plane)

the range of $12 \leq k \leq 72$ W/m·K. This difference is observed because the actual heat supplied is lower than $q_{\text{supp}} < 10$ W, as demonstrated in the analysis using Eqs. (8) and (9). Furthermore, the conduction heat loss through a later (in-plane) direction facilitates the 2D heat transfer phenomenon, which deviates from the 1D Fourier analysis. This thermal conductivity of Al₂O₃/rGO when k is approximately 10^1 W/m·K is considerably higher than that of the rGO layer when k is approximately 10^{-2} W/m·K. Using the guarded hot plate method (heat flux measurement based on ASTM Method E1461), the thermal conductivity of the 100- μ m-thick rGO layer was estimated to be approximately $k_{\text{rGO}} = 0.08$ W/m·K. Thus, the corresponding thermal resistance along the normal direction is approximately $(R_{A_p}) = \Delta x/k_{\text{rGO}} = (1 \times 10^{-4} \text{ m})/(0.08 \text{ W/m·K}) = 1.25 \times 10^{-3} \text{ m}^2\cdot\text{K}/\text{W}$. Hung et al. reported that the thermal conductivity of 1-mm-thick graphite nanoplatelets (GnP) films is $k_{\text{GnP}} = 0.23$ W/m·K, which yields a normal thermal resistance of $\Delta x/k_{\text{GnP}} = 4.35 \times 10^{-3} \text{ m}^2\cdot\text{K}/\text{W}$, which is higher than our value [43]. Raza et al. also reported the thermal conductivity of 10-mm-thick carbon nanofiber films to be $k_{\text{CNF}} = 1.85$ W/m·K, which provides a normal thermal resistance of $\Delta x/k_{\text{CNF}} = 5.4 \times 10^{-3} \text{ m}^2\cdot\text{K}/\text{W}$ [44]. These thermal resistance values are listed in Table 2. The superior “normal” thermal resistance of rGO/AgNW over the values of GnP [43] and carbon nanofiber [44] may be due to the densely packed coating materials supersonic impact, which might have resulted in strong bonding along the normal direction, yielding a relatively low contact resistance.

The thermal resistance of graphene-related materials along a lateral (or “in-plane”) direction is considerably smaller than those along a “normal” direction. The graphene-related materials are known to exhibit superior electrical and thermal properties along an “in-plane” direction while utilizing the superior covalent bonding between the carbon atoms. This bonding structure facilitates highly excited lattice vibration (or phonon) that increases the thermal conductivity [22]. The superior thermal resistances of the graphene-related materials in the range of 10^{-5} – $10^{-6} \text{ m}^2\cdot\text{K}/\text{W}$ are also listed in Table 2.

4. Conclusion

Thin films comprising rGO and AgNWs were fabricated using supersonic spraying. The fabrication of compact rGO–AgNW films was realized via the high-velocity impact of the depositing materials against the Al₂O₃ substrates. The fabricated film was Joule heated using a nickel-chrome wire which created a line-pattern hotspot. With the improved thermal conductivity of the rGO–AgNW hybrid film, heat was quickly dissipated in all directions and the hotspot temperature was quickly reduced. An rGO thickness of about 10 μ m produced the lowest thermal resistance. Pure rGO films of less than 5 μ m thick did not transport sufficient heat, preventing efficient cooling. Film thicknesses greater than 15 μ m were excessive and adversely caused thermal insulation. The addition of AgNWs to rGO decreased the conductive thermal resistance of the film, but was minimally effective in influencing convective heat transfer. Heat-induced malfunctions in power electronics devices may find an efficient way of removing heat using supersonically sprayed rGO–AgNW hybrid films.

Acknowledgement

This research was supported by the Technology Development Program to Solve Climate Changes of the National Research Foundation (NRF) funded by the Ministry of Science, ICT & Future Planning (NRF-2016M1A2A2936760), NRF-2017R1A2B4005639, and NRF-2013R1A5A1073861. This research was also funded by the National Research Council of Science & Technology (NST) grant by the Korea government (MSIP) (No. CRC-16-02-KICT) and KU-FRG (K1822531).

References

- [1] P. Wang, Recent Advance in Thermoelectric Devices for Electronics Cooling, in: Encyclopedia of Thermal Packaging, pp. 145–168.
- [2] P. Wang, A. Bar-Cohen, B. Yang, G.L. Solbrekken, A. Shakouri, Analytical modeling of silicon thermoelectric microcooler, J. Appl. Phys. 100 (1) (2006) 014501.
- [3] R. Mahajan, C. Chia-pin, G. Chrysler, Cooling a microprocessor chip, Proc. IEEE 94 (8) (2006) 1476–1486.
- [4] A. Bar-Cohen, P. Wang, E. Rahim, Thermal management of high heat flux nanoelectronic chips, Microgravity Sci. Technol. 19 (3) (2007) 48–52.
- [5] P. Wang, A. Bar-Cohen, On-chip hot spot cooling using silicon thermoelectric microcoolers, J. Appl. Phys. 102 (3) (2007) 034503.
- [6] A. Majumdar, Thermoelectric devices: helping chips to keep their cool, Nat. Nanotechnol. 4 (4) (2009) 214.
- [7] I. Chowdhury, R. Prasher, K. Lofgreen, G. Chrysler, S. Narasimhan, R. Mahajan, D. Koester, R. Alley, R. Venkatasubramanian, On-chip cooling by superlattice-based thin-film thermoelectrics, Nat. Nanotechnol. 4 (4) (2009) 235.
- [8] C. Wong, K.-S. Moon, Y. Li, Nano-bio-electronic, Photonic and MEMS Packaging, Springer, 2010.
- [9] A. Bar-Cohen, P. Wang, Thermal management of on-chip hot spot, in: ASME 2009 Second International Conference on Micro/Nanoscale Heat and Mass Transfer, American Society of Mechanical Engineers, 2009, pp. 553–567.
- [10] A.L. Moore, L. Shi, Emerging challenges and materials for thermal management of electronics, Mater. Today 17 (4) (2014) 163–174.
- [11] C.S. Sharma, M.K. Tiwari, S. Zimmermann, T. Brunschweiler, G. Schlottig, B. Michel, D. Poulikakos, Energy efficient hotspot-targeted embedded liquid cooling of electronics, Appl. Energy 138 (2015) 414–422.
- [12] P. Wang, A. Bar-Cohen, Self-cooling on germanium chip, IEEE Trans. Compon. Packag. Manuf. Technol. 1 (5) (2011) 705–713.
- [13] S. An, H.S. Jo, S.S. Al-Deyab, A.L. Yarin, S.S. Yoon, Nano-textured copper oxide nanofibers for efficient air cooling, J. Appl. Phys. 119 (6) (2016) 065306.
- [14] Y. Liu, Power Electronic Packaging: Design, Assembly Process, Reliability and Modeling, Springer Science & Business Media, 2012.
- [15] J. Xu, A. Munari, E. Dalton, A. Mathewson, K.M. Razeed, Silver nanowire array-polymer composite as thermal interface material, J. Appl. Phys. 106 (12) (2009) 124310.
- [16] H. Yu, L. Li, T. Kido, G. Xi, G. Xu, F. Guo, Thermal and insulating properties of epoxy/aluminum nitride composites used for thermal interface material, J. Appl. Polym. Sci. 124 (1) (2012) 669–677.
- [17] K. Sanada, Y. Tada, Y. Shindo, Thermal conductivity of polymer composites with close-packed structure of nano and micro fillers, Composites Part A 40 (6–7) (2009) 724–730.
- [18] T. Zhang, B.G. Sammakia, Z. Yang, H. Wang, Hybrid nanocomposite thermal interface materials: the thermal conductivity and the packing density, J. Electron. Packag. 140 (3) (2018) 031006.
- [19] K.M. Shahil, A.A. Balandin, Thermal properties of graphene and multilayer graphene: applications in thermal interface materials, Solid State Commun. 152 (15) (2012) 1331–1340.
- [20] A. Yu, P. Ramesh, M.E. Itkis, E. Bekyarova, R.C. Haddon, Graphite nanoplatelet-epoxy composite thermal interface materials, J. Phys. Chem. C 111 (21) (2007) 7565–7569.
- [21] M.A. Peacock, C.K. Roy, M.C. Hamilton, R.W. Johnson, R.W. Knight, D.K. Harris, Characterization of transferred vertically aligned carbon nanotubes arrays as thermal interface materials, Int. J. Heat Mass Transfer 97 (2016) 94–100.
- [22] R. Prasher, Graphene spreads the heat, Science 328 (5975) (2010) 185–186.
- [23] H. Malekpour, K.-H. Chang, J.-C. Chen, C.-Y. Lu, D. Nika, K. Novoselov, A. Balandin,

- Thermal conductivity of graphene laminate, *Nano Lett.* 14 (9) (2014) 5155–5161.
- [24] F. Kargar, Z. Barani, R. Salgado, B. Debnath, J.S. Lewis, E. Aytan, R.K. Lake, A.A. Balandin, Thermal percolation threshold and thermal properties of composites with high loading of graphene and boron nitride fillers, *ACS Appl. Mater. Interfaces* 10 (43) (2018) 37555–37565.
- [25] F. Kargar, Z. Barani, M. Balinskiy, A.S. Magana, J.S. Lewis, A.A. Balandin, Dual-Functional Graphene Composites for Electromagnetic Shielding and Thermal Management, *Adv. Electron. Mater.* 5 (1) (2019) 1800558.
- [26] J.S. Lewis, Z. Barani, A.S. Magana, F. Kargar, A.A. Balandin, Thermal and electrical conductivity control in hybrid composites with graphene and boron nitride fillers, *Mater. Res. Express* 6 (8) (2019) 085325.
- [27] A.A. Balandin, S. Ghosh, W. Bao, I. Calizo, D. Teweldebrhan, F. Miao, C.N. Lau, Superior thermal conductivity of single-layer graphene, *Nano Lett.* 8 (3) (2008) 902–907.
- [28] J.H. Seol, I. Jo, A.L. Moore, L. Lindsay, Z.H. Aitken, M.T. Pettes, X. Li, Z. Yao, R. Huang, D. Broido, Two-dimensional phonon transport in supported graphene, *Science* 328 (5975) (2010) 213–216.
- [29] G.-C. He, H. Lu, X.-Z. Dong, Y.-L. Zhang, J. Liu, C.-Q. Xie, Z.-S. Zhao, Electrical and thermal properties of silver nanowire fabricated on a flexible substrate by two-beam laser direct writing for designing a thermometer, *RSC Adv.* 8 (44) (2018) 24893–24899.
- [30] R. Chen, S.R. Das, C. Jeong, M.R. Khan, D.B. Janes, M.A. Alam, Co-percolating graphene-wrapped silver nanowire network for high performance, highly stable, transparent conducting electrodes, *Adv. Func. Mater.* 23 (41) (2013) 5150–5158.
- [31] S.R. Das, Q. Nian, M. Saei, S. Jin, D. Back, P. Kumar, D.B. Janes, M.A. Alam, G.J. Cheng, Single-layer graphene as a barrier layer for intense UV laser-induced damages for silver nanowire network, *ACS Nano* 9 (11) (2015) 11121–11133.
- [32] K. Maize, S.R. Das, S. Sadeque, A.M. Mohammed, A. Shakouri, D.B. Janes, M.A. Alam, Super-Joule heating in graphene and silver nanowire network, *Appl. Phys. Lett.* 106 (14) (2015) 143104.
- [33] D.Y. Kim, S. Sinha-Ray, J.J. Park, J.G. Lee, Y.H. Cha, S.H. Bae, J.H. Ahn, Y.C. Jung, S.M. Kim, A.L. Yarin, Self-healing reduced graphene oxide films by supersonic kinetic spraying, *Adv. Func. Mater.* 24 (31) (2014) 4986–4995.
- [34] J.G. Lee, D.-Y. Kim, J.-H. Lee, M.-W. Kim, S. An, H.S. Jo, C. Nervi, S.S. Al-Deyab, M.T. Swihart, S.S. Yoon, Scalable binder-free supersonic cold spraying of nano-textured cupric oxide (CuO) films as efficient photocathodes, *ACS Appl. Mater. Interfaces* 8 (24) (2016) 15406–15414.
- [35] J.-G. Lee, J.-H. Lee, S. An, D.-Y. Kim, T.-G. Kim, S.S. Al-Deyab, A.L. Yarin, S.S. Yoon, Highly flexible, stretchable, wearable, patternable and transparent heaters on complex 3D surfaces formed from supersonically sprayed silver nanowires, *J. Mater. Chem. A* 5 (14) (2017) 6677–6685.
- [36] J.G. Lee, D.Y. Kim, J.H. Lee, S. Sinha-Ray, A.L. Yarin, M.T. Swihart, D. Kim, S.S. Yoon, Production of flexible transparent conducting films of self-fused nanowires via one-step supersonic spraying, *Adv. Func. Mater.* 27 (1) (2017) 1602548.
- [37] J.-G. Lee, S. An, T.-G. Kim, M.-W. Kim, H.-S. Jo, M.T. Swihart, A.L. Yarin, S.S. Yoon, Self-cleaning anticondensing glass via supersonic spraying of silver nanowires, silica, and polystyrene nanoparticles, *ACS Appl. Mater. Interfaces* 9 (40) (2017) 35325–35332.
- [38] J.G. Lee, D.Y. Kim, T.G. Kim, J.H. Lee, S.S. Al-Deyab, H.W. Lee, J.S. Kim, D.H. Yang, A.L. Yarin, S.S. Yoon, Supersonically sprayed copper-nickel microparticles as flexible and printable thin-film high-temperature heaters, *Adv. Mater. Interfaces* 4 (17) (2017) 1700075.
- [39] S.J. Kline, Describing uncertainty in single sample experiments, *Mech. Eng.* 75 (1953) 3–8.
- [40] A.C. Ferrari, J. Robertson, Interpretation of Raman spectra of disordered and amorphous carbon, *Phys. Rev. B* 61 (20) (2000) 14095.
- [41] Z. Luo, Z. Cai, Y. Wang, Y. Wang, B. Wang, In situ growth of silver nanowires on reduced graphene oxide sheets for transparent electrically conductive films, *RSC Adv.* 6 (43) (2016) 37124–37129.
- [42] A.K. Nair, N. Kalarikkal, S. Thomas, M. Kala, V. Sahajwalla, R.K. Joshi, S. Alwarappan, Boron doped graphene wrapped silver nanowires as an efficient electrocatalyst for molecular oxygen reduction, *Sci. Rep.* 6 (2016) 37731.
- [43] M.-T. Hung, O. Choi, Y.S. Ju, H. Hahn, Heat conduction in graphite-nanoplatelet-reinforced polymer nanocomposites, *Appl. Phys. Lett.* 89 (2) (2006) 023117.
- [44] M.A. Raza, A. Westwood, C. Stirling, Effect of processing technique on the transport and mechanical properties of vapour grown carbon nanofibre/rubbery epoxy composites for electronic packaging applications, *Carbon* 50 (1) (2012) 84–97.
- [45] C. Lin, D. Chung, Graphite nanoplatelet pastes vs. carbon black pastes as thermal interface materials, *Carbon* 47 (1) (2009) 295–305.
- [46] M. Raza, A. Westwood, C. Stirling, Graphite nanoplatelet/silicone composites for thermal interface applications, in: *2010 International Symposium on Advanced Packaging Materials: Microtech (APM), IEEE, 2010, pp. 34–48.*
- [47] K. Hu, D. Chung, Flexible graphite modified by carbon black paste for use as a thermal interface material, *Carbon* 49 (4) (2011) 1075–1086.